



Changes in obliquity drive tree cover shifts in eastern tropical South America

Jaqueline Q. Ferreira ^{a, b, *}, Cristiano M. Chiessi ^a, Marina Hirota ^c, Rafael S. Oliveira ^d, Matthias Prange ^e, Christoph Häggi ^{f, g}, Stefano Crivellari ^a, Sri D. Nandini-Weiss ^e, Dailson J. Bertassoli Jr. ^a, Marília C. Campos ^b, Stefan Mulitza ^e, Ana Luiza S. Albuquerque ^h, André Bahr ⁱ, Enno Schefuß ^e

^a School of Arts, Sciences and Humanities, University of São Paulo, São Paulo, Brazil

^b Institute of Geosciences, University of São Paulo, São Paulo, Brazil

^c Department of Physics, Federal University of Santa Catarina, Florianópolis, Brazil

^d Department of Plant Biology, University of Campinas, Campinas, Brazil

^e MARUM – Center for Marine Environmental Sciences, University of Bremen, Bremen, Germany

^f Department of Earth Sciences, University of Southern California, Los Angeles, USA

^g Geological Institute, ETH Zurich, Zurich, Switzerland

^h Graduate Program on Geosciences (Geochemistry), Fluminense Federal University, Niterói, Brazil

ⁱ Institute of Earth Sciences, Heidelberg University, Heidelberg, Germany

ARTICLE INFO

Article history:

Received 19 July 2021

Received in revised form

20 January 2022

Accepted 22 January 2022

Available online xxx

Handling Editor: Prof. C. Hillaire-Marcel

Keywords:

Quaternary

South America

Vegetation

Orbital forcing

Long chain *n*-alkanes

Precipitation

ABSTRACT

Despite its great ecological importance, the main factors governing tree cover in tropical savannas as well as savanna-forest boundaries are still largely unknown. Here we address this issue by investigating marine sediment records of long-chain *n*-alkane stable carbon ($\delta^{13}\text{C}_{\text{wax}}$) and hydrogen ($\delta\text{D}_{\text{wax}}$) isotopes from a core collected off eastern tropical South America spanning the last ca. 45 thousand years. While $\delta^{13}\text{C}_{\text{wax}}$ is a proxy for the main photosynthetic pathway of terrestrial vegetation, tracking the relative proportion of C_3 (mainly trees) versus C_4 (mainly grasses) plants, $\delta\text{D}_{\text{wax}}$ is a proxy for continental precipitation, tracking the intensity of rainfall. The investigated core was collected off the mouth of the São Francisco River drainage basin, a tropical savanna-dominated region with dry austral autumn, winter and spring. On top of millennial-scale changes, driven by anomalies in the amount of precipitation associated with Heinrich Stadials, we identify a marked obliquity control over the expansion and contraction of tree and grass cover. During periods of maximum (minimum) obliquity, trees (grasses) reached maximum coverage. We suggest that maximum (minimum) obliquity decreased (increased) the length of the dry season allowing (hampering) the expansion of tree-dominated vegetation. Periods of maximum obliquity induced an anomalous heating (cooling) of the summer (winter) hemisphere that in combination with a delayed response of the climate system slightly increased autumn precipitation over the São Francisco River drainage basin, through a shift of the Intertropical Convergence Zone towards or further into the anomalously heated hemisphere. We found that atmospheric CO_2 concentration has only a secondary effect on tree cover. Our results underline the importance of the dry season length as a governing factor in the long-term control of tree cover in tropical landscapes.

© 2022 Elsevier Ltd. All rights reserved.

1. Introduction

Tropical savannas can be defined as tree-grass systems, with

discontinuous woody cover above a semi-continuous or continuous grass layer (House et al., 2003; Sankaran et al., 2004). These ecosystems are present across a wide range of climate conditions (House et al., 2003) and have enormous socioeconomic relevance since they cover substantial areas and act as biodiversity hotspots (Myers et al., 2000). Tree cover density is highly variable in different savanna types, and several factors including the availability of

* Corresponding author. School of Arts, Sciences and Humanities, University of São Paulo, São Paulo, Brazil.

E-mail address: jaqueline.q.ferreira@gmail.com (J.Q. Ferreira).

nutrients and water, as well as the action of fire and herbivores may influence this parameter (Bond, 2008; Bond and Keeley, 2005; Staver et al., 2011). Additionally, changes in atmospheric CO₂ concentration might exert a significant control in tree-grass distribution in tropical and subtropical savanna ecosystems, since higher CO₂ concentration favor trees (e.g., Ehleringer et al., 1997; Bragg et al., 2013).

The proportion of tree cover has a profound ecological importance for tropical savannas. For instance, with the increase of canopy density, grass production usually declines (Bond and Keeley, 2005). The closed canopy reduces the flammability of the ecosystem, directly reducing fire spread (Hoffmann et al., 2012). In addition, tree cover density in tropical savannas also intensely impacts herbivore communities (Riginos and Grace, 2008), as well as the carbon and hydrological cycles (Jackson et al., 2002; Simioni et al., 2003).

The factors responsible for tree density in tropical savannas can be analogous to those that control the distribution of tropical savannas and forests (Hirota et al., 2011; Hoffmann et al., 2012). These two vegetation types usually occur alongside each other and have been characterized as alternative stable states (Hirota et al., 2010, 2011; Staver et al., 2011). However, the environmental conditions that support a specific tree cover state (i.e., fire, precipitation, soil) and the aspects that define its variability, are still largely unknown (House et al., 2003; Hoffmann et al., 2012). Also, ecological models used to predict the tropical savanna to forest transition fall short in mimicking the entire complexity of natural ecosystems and are not fully able to capture its environmental long-term impacts (Pausas and Bond, 2020).

Paleoenvironmental records can substantially contribute to a better understanding of the factors controlling tree cover in tropical ecosystems (Cerling et al., 2011). The stable isotope compositions of long chain *n*-alkanes of terrestrial higher plants have been successfully used to reconstruct ancient ecosystems and precipitation (e.g., Collins et al., 2011; Schefuß et al., 2011; Dubois et al., 2014; Häggi et al., 2017). These organic compounds are transported both by rivers and winds to the oceans, providing records of past continental environments (Bird et al., 1995). The stable isotope composition of carbon ($\delta^{13}\text{C}$) in long chain *n*-alkanes indicates the main photosynthetic pathway of vegetation, allowing the assessment of the relative proportion of trees (C₃ photosynthetic pathway) and grasses (C₄ photosynthetic pathway) (Schefuß et al., 2005). The stable isotope composition of hydrogen (δD) can be related to the hydrogen-isotopic composition of precipitation (Sachse et al., 2012). In the tropics, precipitation is characterized by limited re-evaporation during high-intensity rainfall events, which, according to observational and modelling studies, favors the inclusion of the light isotope to the precipitated water (Lee and Fung, 2008; Risi et al., 2008). Hence, an increase in rainfall intensity can be correlated with decreased values of δD in plant-waxes (Dansgaard, 1964; Sachse et al., 2012).

In order to assess the vegetation response from eastern tropical South America to hydroclimate changes during the last ca. 45 kyr, we analyzed a marine sediment core that archived sediments from the São Francisco River drainage basin (SFRB), the largest basin in eastern tropical South America (Fig. 1). We used $\delta^{13}\text{C}$ and δD of long-chain *n*-alkanes to reconstruct regional vegetation composition and precipitation dynamics, respectively. In addition, we used the fully coupled Community Earth System Model (CESM, version 1.2.2) to assess potential changes in precipitation seasonality that could impact past vegetation patterns. Our findings show enhanced tree cover during periods of decreased dry season length (DSL). This shift in vegetation composition shows no primary relation with changes in atmospheric CO₂ concentration, indicating that hydrological variations are the driving factor in tree cover. We found that

the variation in obliquity of Earth's axis control the DSL in eastern tropical South America. In addition, we show that even subtle changes in modern DSL affect tree density in the SFRB.

2. Regional setting

The SFRB (ca. 7–22° S, 48–36° W) is the largest river basin in eastern South America (Fig. 1; Fig. S1) with an annual mean water discharge of around 2.800 m³/s (ANA - Agência Nacional de Águas - Superintendência de Planejamento de Recursos Hídricos, 2015). Precipitation in the southern portion of the SFRB mainly occurs during austral summer (December–February), when the moisture transported by the NE trade winds allows the development of the South American Monsoon System (SAMS) (Vera et al., 2006). The main convective activity of the SAMS is placed over western Brazil and extends in a NW-SE elongated convective belt over southeastern South America and the adjacent western South Atlantic, forming the South Atlantic Convergence Zone (SACZ) (Carvalho et al., 2004). In the southern portion of the SFRB, mean annual precipitation reaches 2000 mm/yr with a DSL (i.e., the number of months with mean precipitation lower than 100 mm/month; Nix, 1983) of 6–7 months. In the upper troposphere, the convective activity associated with the SAMS produces the Bolivian High over the Altiplano that is dynamically linked to the Nordeste Low over northeastern Brazil (Lenters and Cook, 1997). The Nordeste Low, in turn, produces large-scale subsidence over northeastern Brazil that affects the northern portion of the SFRB, where mean annual precipitation is lower than 500 mm/yr and the DSL is about 11 months. Between these two extremes, the central SFRB shows mean annual precipitation of ca. 1200 mm/yr and a DSL of 6–10 months. Over a narrow strip along the coast of northeastern Brazil, rainfall maximum occurs during austral autumn and winter. It is associated with sea breeze circulation (Kousky, 1979), as well as to the occurrence of easterly wave disturbances in the wind field, which locally increase low-level convergence and rainfall (Gomes et al., 2015). This feature affects the mouth of the SFRB.

The Atlantic Forest biome occurs over the southern portion of the SFRB and along a narrow coastal strip on the coast of northeastern Brazil (Fig. 1c), covering ca. 5% of the SFRB (Souza et al., 2020). This biome comprises two major vegetation types: the Atlantic Rain Forest, which runs along the coastline of northeastern Brazil, and the Atlantic Semi-deciduous Forest, which occupies higher elevation inland areas over the southern portion of the SFRB (Oliveira-Filho and Fontes, 2000). The northern portion of the SFRB is covered by the Caatinga biome (ca. 50% of the SFRB), composed of a mosaic of tropical dry forests and shrublands, with the occurrence of xerophytic, woody, thorny and deciduous structures (Sampaio, 1995). Between these very distinct biomes, the Cerrado biome occupies a vast central portion of the SFRB (ca. 45% of the SFRB). The Cerrado is a complex ecosystem with mixed trees and grasses, ranging from tree-less open vegetation (Campo Limpo) with a dense ground cover and small shrubs, to a closed canopy with a dense occurrence of trees (Cerradão) and associated gallery forests following the watercourses (Bridgewater et al., 2004). The Cerrado and Caatinga formations act as a corridor separating the Atlantic Forest (to the SE of the SFRB) from the Amazonian Forest (to the NW of the SFRB).

In this study, we differentiate current vegetation based on the MapBiomas classification system (Souza et al., 2020). Vegetation types dominated by tree species with high-density continuous canopy were defined as forest formations. Vegetation types with a varying density of trees distributed over a continuous shrub-herbaceous layer were defined as savanna formations. Vegetation types with no trees and the predominance of an herbaceous layer are defined as grassland formations (Fig. 1c) (Souza et al., 2020).

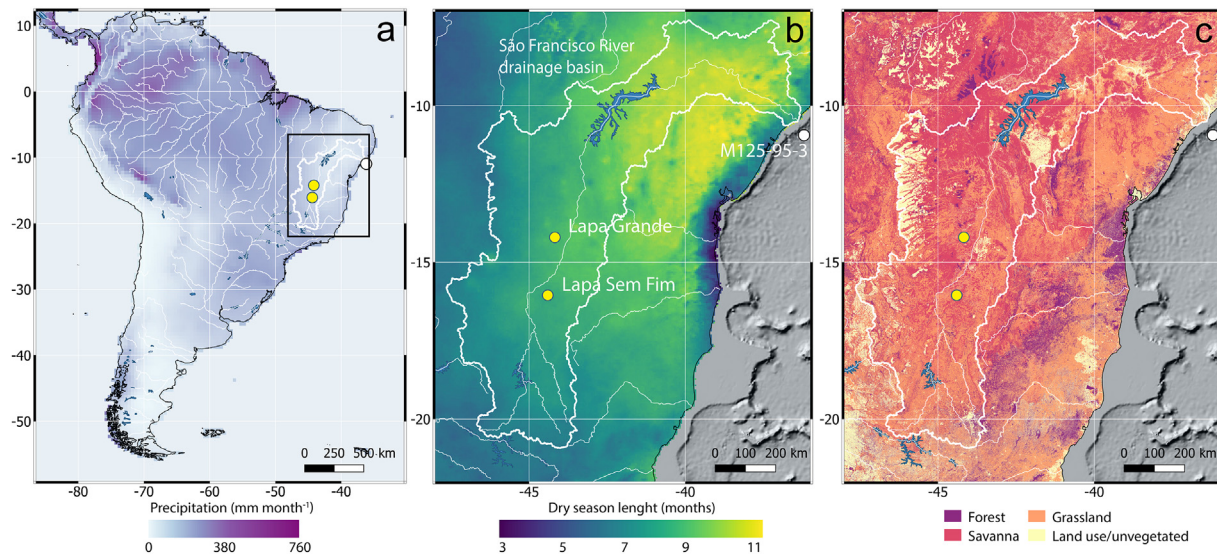


Fig. 1. Climatological and ecological features of the São Francisco River drainage basin and adjacent areas (7–22° S, 48–36° W). (a) Mean annual precipitation (Harris et al., 2020). (b) Dry season length (Funk et al., 2015). (c) Current distribution of tropical forest, savanna and grassland formations based on MapBiomas land cover data (Souza et al., 2020). The black rectangle in (a) depicts the area shown in (b) and (a). The location of marine sediment core M125-95-3 (this study) is indicated by a white circle. The locations of the Lapa Grande and Lapa Sem Fim speleothem records (Strikis et al., 2018) are indicated by yellow circles. (For interpretation of the references to color in this figure legend, the reader is referred to the Web version of this article.)

3. Material and methods

3.1. Marine sediment core and geoinformation

We investigated marine sediment core M125-95-3 (10.94° S, 36.20° W; 1897 m water depth; 10.4 m core length) collected off the São Francisco River mouth in the eastern South American continental slope (Fig. 1) during RV Meteor cruise M125 (Bahr et al., 2016). For geostatistical analyses, the following geographic information was used: (i) mean annual precipitation and DSL calculated from monthly Climate Hazard group Infrared Precipitation with Stations (CHIRPS) precipitation data covering the 1981–2017 period (Funk et al., 2015); and (ii) distribution of vegetation formations (i.e., forest, savanna, grassland) and land use data from MapBiomas (Souza et al., 2020).

3.2. Age model

Nine calibrated ^{14}C accelerator mass spectrometry ages performed on planktonic foraminifera and three benthic foraminifera oxygen isotopic composition tie-points were used to produce the age model of core M125-95-3 (Campos et al., 2019). Absolute ^{14}C ages were calibrated with the IntCal20 calibration curve (Reimer et al., 2020) and a variable simulated reservoir age from the transient modeling experiments described in Butzin et al. (2017). The benthic foraminifera oxygen isotopic reference curve from Govin et al. (2014) was used to establish additional tie-points. The age modeling algorithm BACON v. 2.2 (Blaauw and Christeny, 2011) was used within the software PaleoDataView v. 0.9.5.4 (Langner and Mülitz, 2019) to construct the age model. The investigated section of core M125-95-3 (i.e., uppermost 470 cm) covers the last ca. 45 kyr and shows an average sedimentation rate of 10.4 cm/kyr. Further details regarding the age model are provided in Campos et al. (2019).

3.3. Lipids extraction and compound isolation

Freeze-dried (Christ Beta 1–8 LDplus) sediment samples (ca. 6 g) were ground with an agate pestle and mortar. A squalane internal standard was added to the samples before extraction. Lipid compounds were extracted with a DIONEX Accelerated Solvent Extractor (ASE200) at 100 °C and 1000 psi using a dichloromethane methanol (DCM:MeOH 9:1 v/v) solution, for three cycles of 5 min each. The solvent was removed by rotary evaporation (Heidolph ROTOVAP system) to near dryness and elemental sulfur was removed from the extracts using copper turnings. Lipid extracts were saponified using 0.1M potassium hydroxide (KOH) in a MeOH solution at 85 °C for 2 h and the neutral fraction was extracted with hexane. The neutral fraction was split into fractions of different polarity using a deactivated silica (1% H₂O) column. The column was eluted with hexane, DCM and DCM:MeOH (1:1), yielding the *n*-alkane, ketone and polar fractions. Unsaturated hydrocarbons were removed from the *n*-alkane fractions by elution over 4 cm of AgNO₃-coated silica using hexane as solvent.

3.4. *n*-Alkane quantification

The *n*-alkane fraction was analyzed in a Thermo Fisher Scientific Focus gas chromatograph (GC) equipped with an Rxi5 ms 30 x column (30 m, 0.25 mm, 0.25 mm) and a flame ionization detector (FID). To quantify the *n*-alkane concentrations, the resulting peak areas were manually integrated and compared with an external standard mixture of 16 *n*-alkanes, that was run every six samples. Precision of compound quantification is about 5% based on multiple standard analyses. The carbon preference index (CPI) provides information about the predominance of odd over even carbon numbered molecular chain (Cranwell, 1981), which is used to detect degraded material. We calculate the CPI with the following equation (1):

$$CPI_{27-33} = 0.5 * \left(\frac{nC_{27} + nC_{29} + nC_{31} + nC_{33}}{nC_{26} + nC_{28} + nC_{30} + nC_{32}} + \frac{nC_{27} + nC_{29} + nC_{31} + nC_{33}}{nC_{28} + nC_{30} + nC_{32} + nC_{34}} \right) \quad (1)$$

3.5. Compound-specific isotope analyses

Compound-specific δD analyses (C_{29} and C_{31} *n*-alkanes) were carried out by gas chromatography-isotope ratio mass spectrometry (GC-IRMS) with a Thermo Fisher Scientific MAT 253 coupled via a GC Isolink operated at 1420 °C to a Thermo Fisher Scientific Trace GC. δD compositions were measured against a calibrated H_2 reference gas. Isotope values are reported in ‰ versus Vienna Standard Mean Ocean Water (VSMOW). The H_3 factor was determined daily and gave values of 5.8 ± 0.2 . An external *n*-alkane standard mixture calibrated against the A4-Mix isotope standard (A. Schimmelmann, Indiana University) was measured every sixth analysis. Precision for replicate measurements ranged between 0‰ and 5‰ for both homologues.

Compound-specific $\delta^{13}C$ analyses (C_{29} and C_{31} *n*-alkanes) were performed by GC-IRMS on a Thermo Fisher Scientific MAT 252 coupled via a GC combustion interface with a nickel catalyzer operated at 1000 °C to a Thermo Fisher Scientific Trace GC. $\delta^{13}C$ compositions were measured against a calibrated CO_2 reference gas. Isotope values are reported in ‰ versus Vienna Pee Dee Belemnite (VPDB). An external *n*-alkane standard mixture calibrated against the A4-Mix isotope standard (A. Schimmelmann, Indiana University) was measured every sixth analysis. Precision for replicate measurements ranged between 0‰ and 0.3‰ for both homologues.

Accuracy for each measurement was controlled using the internal squalane standard, which yielded average deviations of 2.0‰ for δD and 0.1‰ for $\delta^{13}C$ from their target value. Long-term mean absolute deviation based on the external *n*-alkane standard mixture was 3.0‰ for δD and 0.3‰ for $\delta^{13}C$.

3.6. Ice volume correction

Global mean seawater was isotopically heavier during the last glacial compared to the present interglacial due to the larger ice volume (Schrag et al., 2002). We removed the effect of changing ice volume on the isotopic composition of δD using the following equation (2) (Tierney and DeMenocal, 2013):

$$\delta D_{wax-IVC} = \frac{1000 + \delta D_{wax}}{8 * 0.001 * \delta^{18}O_{isoice} + 1} - 1000 \quad (2)$$

where $\delta D_{wax-IVC}$ is the ice volume corrected isotope values, δD_{wax} is the measured plant-wax values and $\delta^{18}O_{isoice}$ is the effect of ice volume on the benthic $\delta^{18}O$ variation according to Bintanja et al. (2005).

3.7. Geoinformation processing

We used the MapBiomas database (spatial resolution 30 m × 30 m) to extract the current occurrence of forest, savanna and grassland formations in the area 7–22° S, 48–36° W that encompasses the SFRB (Fig. 1) (Souza et al., 2020). We chose to analyze an area that is slightly larger than the SFRB in order to have a more representative area covered by forest formations, since this

vegetation types currently covers a small area of the basin (Fig. 1c). Because MapBiomas allows the identification and exclusion of areas with strong human-driven change, we were able to filter out the intense human interference in the SFRB.

Mean monthly precipitation values were extracted from the CHIRPS database (Funk et al., 2015), and refer to mean values for the interval 1981–2017. We selected data for the same box that covers the original SFRB area (7–22° S, 48–36° W). We filtered out areas with mean annual precipitation <1000 mm/yr, since the bi-stability range of tropical forests and savannas in the neotropics was characterized to occur between 1000 and 2500 mm (Staver et al., 2011). DSL is defined as the number of months with precipitation <100 mm/month (Nix, 1983).

3.8. Climate model experiments

The climate model used for this study is the fully coupled Community Earth System Model (CESM, version 1.2.2) (Hurrell et al., 2013). The atmosphere component (CAM4) uses a finite volume grid with a 1.9° × 2.5° horizontal resolution, which is shared with the land model grid. The atmosphere grid has 26 layers. The ocean and sea ice models run with a nominal 1° horizontal resolution, where the ocean grid has 60 levels. Two idealized model experiments were performed with maximum (23.98°) obliquity (O_{max}) and minimum (22.59°) obliquity (O_{min}). Eccentricity was set to zero. The experiments were branched from a spun-up standard pre-industrial control simulation following the Paleoclimate Modelling Intercomparison Project 3 (PMIP3) (Braconnot et al., 2012) and run for 300 years each. Averages from the last 50 years of each experiment were taken for the analysis. The results are presented as maximum minus minimum obliquity ($O_{max} - O_{min}$).

4. Results

Long-chain *n*-alkanes CPI_{27-33} values range from 1.7 to 4.9 (median 3.8, inter quartile range 1.0), indicating that the long-chain *n*-alkanes are derived from relatively undegraded terrestrial higher plants. The δD_{29} values vary between –164 and –124‰ (average –145 ± 2‰), and the δD_{31} values vary between –165 and –118‰ (average –152 ± 2‰) (Fig. 2a). Both datasets (i.e., δD_{29} and δD_{31}) show similar changes with an average offset of 6 ± 2‰ (i.e., δD_{29} values are systematically higher than δD_{31} values) from the base of the record until ca. 12.5 ka BP. During the Holocene, the δD_{29} values do not show major changes while the δD_{31} values show a multi-millennial increasing trend. δD_{wax} (i.e., weighted average of δD_{29} and δD_{31} values) shows an average of –151 ± 2‰ during the last glacial and –136 ± 2‰ during the Holocene (Fig. 3d). The δD_{wax} record does not show a clear orbital trend, but shows substantial millennial-scale negative excursions, that coincide with Heinrich Stadial (HS) 4 (range of –16‰), HS3 (range of –12‰), HS2 (range of –15‰) and HS1 (range of –29‰). The millennial-scale negative excursions are present in both δD_{29} and δD_{31} records.

The $\delta^{13}C_{29}$ values range from –31.1 to –28.9‰ (average –30.1 ± 0.2‰), and the $\delta^{13}C_{31}$ ranges from –30.1 to –26.9‰ (average –28.6 ± 0.2‰) (Fig. 2b). The isotopic difference between homologues ($\Delta\delta^{13}C_{31-29}$) varies between 0.8‰ and 2‰

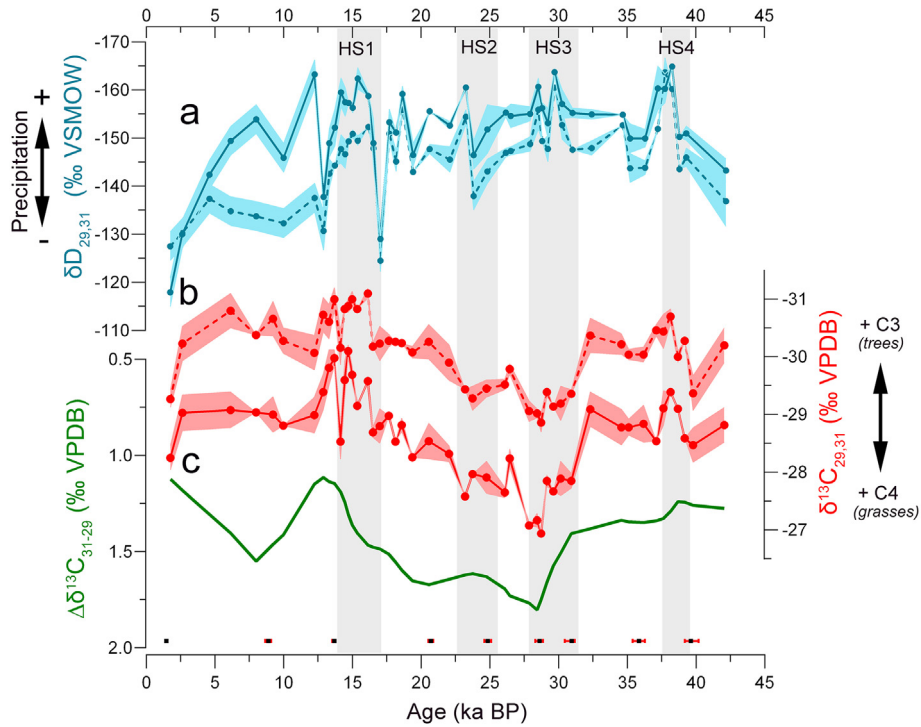


Fig. 2. Stable hydrogen (δD) and carbon ($\delta^{13}C$) isotope records of long-chain *n*-alkanes from marine sediment core M125-95-3 for the last ca. 45 kyr. (a) Ice volume corrected δD_{29} (dashed line) and δD_{31} (continuous line) values recording changes in precipitation over the São Francisco River drainage basin (SFRB). (b) $\delta^{13}C_{29}$ (dashed line) and $\delta^{13}C_{31}$ (continuous line) values recording changes in the relative abundance of C_3 versus C_4 vegetation in the SFRB. (c) Locally estimated scatterplot smoothing (LOESS) $\delta^{13}C$ difference between homologues C_{31} and C_{29} ($\Delta\delta^{13}C_{31-29}$) [smoothing factor = 0.2]. Calibrated ^{14}C accelerator mass spectrometry ages with 2 sigma error of core M125-95-3 are indicated by squares on the lower axis. The grey bars indicate Heinrich Stadials (HS) 4 to 1. Shaded areas in the isotope records indicate the standard deviation of isotope values based on replicate analyses.

(average $1.4 \pm 0.3\text{‰}$) (Fig. 2c), both datasets (i.e., $\delta^{13}C_{29}$ and $\delta^{13}C_{31}$) show similar changes (i.e., $\delta^{13}C_{29}$ values are systematically lower than $\delta^{13}C_{31}$ values) throughout the investigated section of the core. $\delta^{13}C_{wax}$ (i.e., weighted average of δC_{29} and δC_{31} values) shows an average of $-29.4 \pm 0.2\text{‰}$ (Fig. 3e). The record shows an orbital-scale quasi-sinusoidal trend, with most enriched values of $-27.9 \pm 0.2\text{‰}$ at ca. 29.0 ka BP, and most depleted values of $-30.5 \pm 0.2\text{‰}$ at ca. 15.0 ka BP.

According to values extracted from the CHIRPS database, the modern median DSL of the region covered by savanna formations in the area 7–22° S, 48–36° W that encompasses the SFRB is 7.4 ± 0.4 months and the modern median DSL of the region covered by forest formations is 7.0 ± 0.5 months (Fig. 4). After confirming non-normality of our sample using the Shapiro-Wilk test, we applied the Mann-Whitney-Wilcoxon test to check whether the DSL distributions of savannas and forests formations were different. The result indicates that the DSL values for forests and savannas formations are significantly different ($N = 4390$; $W = 1011581$; $p < 2.2e-16$).

The CESM experiments ($O_{max} - O_{min}$) show a weak effect of changes in obliquity over SFRB precipitation both in the annual mean and during austral spring (September–November) (Fig. 5a, c). Positive precipitation anomalies occur in the SFRB during austral autumn (March–May) (Fig. 5b).

5. Discussion

5.1. Orbital-scale forcing

Despite the strong control that precession exerts over the strength of the SAMS (e.g., Cruz et al., 2005; Hou et al., 2020) neither our δD_{wax} nor our $\delta^{13}C_{wax}$ records show this type of orbital

spacing (Fig. 3d, e, g) (note that austral summer insolation at the latitudinal range of the SFRB is positively related to precession). An increase in austral summer precipitation induced by the increase in austral summer insolation (Fig. 3g) would be noted in our record, since δD_{wax} mainly reflects rainfall intensity during the wet season. We suggest that the lack of a precession signal is due to the location of the SFRB. Over lowland tropical South America, changes in the strength of the SAMS related to precession produce a precipitation antiphase between northeastern Brazil and the rest of lowland tropical South America (Cruz et al., 2009; Prado et al., 2013). At the transition between these two domains, a signal that integrates large areas of the SFRB (as captured by our isotopic records) does not show a precession pacing (Fig. 3d, g). When the southern portion of the basin is influenced by a strong SAMS (i.e., high austral summer insolation), its northern portion experiences deficit in precipitation, and vice-versa. Indeed, speleothem-based hydroclimate records from the central SFRB (Strikis et al., 2018) as well as the $\ln(Ti/Ca)$ record from marine core M125-95-3 (Campos et al., 2019) do not show a clear precession signal either, agreeing with our δD_{wax} record (Fig. 3b, c, d).

While our δD_{wax} record shows no orbital signal, our $\delta^{13}C_{wax}$ record shows a prominent obliquity pacing (Fig. 3e, f). To our knowledge, an obliquity pacing has not been reported in paleo-environmental records from lowland tropical South America (see Supplementary Material; Fig. S2, S3; Table S1). Under maximum obliquity, negative (positive) insolation anomalies occur in the mid to low (high to mid) latitudes of the winter (summer) hemisphere. This heating contrast between the anomalously warmer summer hemisphere and the anomalously colder winter hemisphere generates dynamical responses in atmospheric circulation (Lee and Poulsen, 2005; Raymo and Nisancioglu, 2003). In order to balance the changes in incoming energy, there is a strengthening

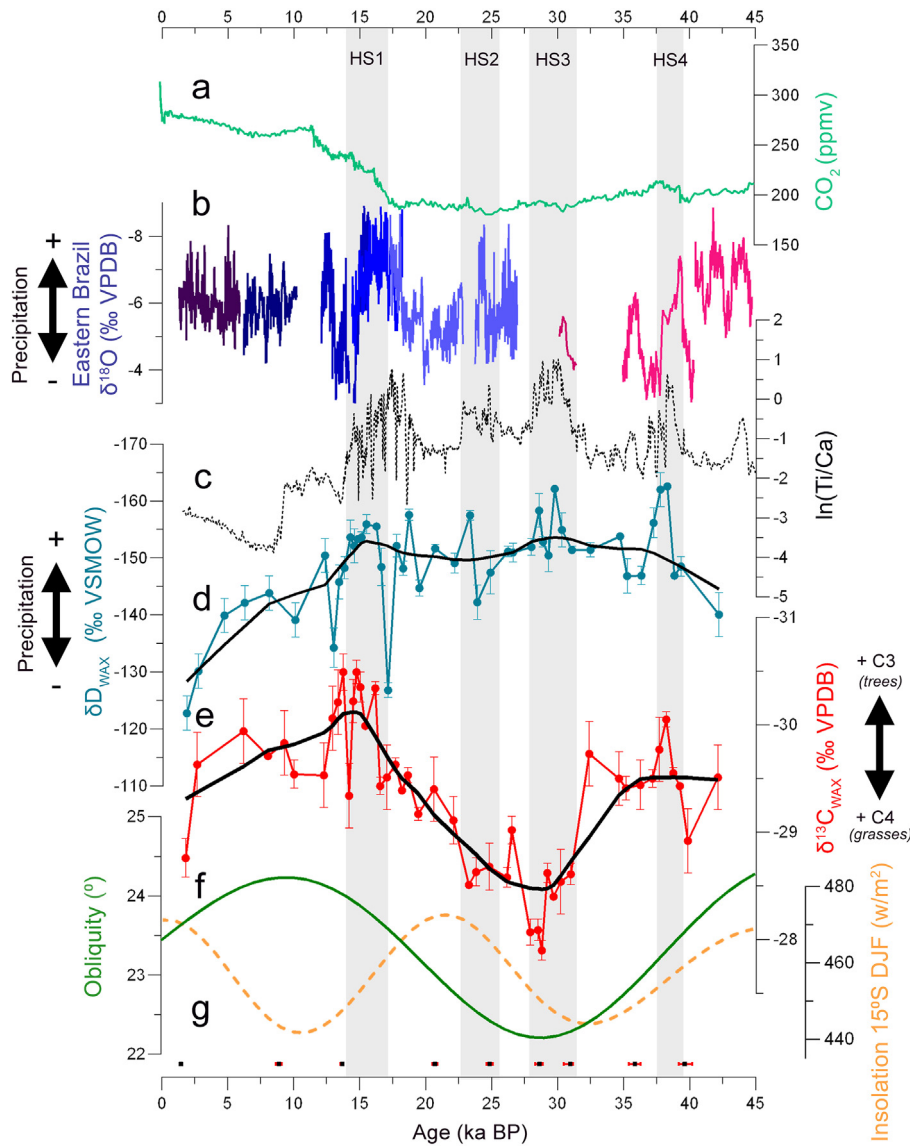


Fig. 3. Precipitation and vegetation reconstructions for the São Francisco River drainage basin for the last ca. 45 kyr. (a) Stacked reconstruction of atmospheric CO₂ concentration (green continuous line) (Bereiter et al., 2015). (b) Speleothem stable oxygen isotope record (δ¹⁸O) from eastern Brazil (different colors indicate different speleothems) (Strikis et al., 2018). (c) ln(Ti/Ca) data of core M125-95-3 (Campos et al., 2019). (d) Long-chain *n*-alkane stable hydrogen isotope record (δD_{wax}) of marine sediment core M125-95-3 representing weighted average values between C₂₉ and C₃₁ *n*-alkanes (blue dashed line) (this study; the locally estimated scatterplot smoothing (LOESS) record of the δD_{wax} data [smoothing factor 0.3] is shown as the bold blue continuous line). (e) Long-chain *n*-alkane stable carbon isotope record (δ¹³C_{wax}) of core M125-95-3 representing weighted average values between C₂₉ and C₃₁ *n*-alkanes (this study; the LOESS record of the δ¹³C_{wax} data [smoothing factor 0.3] is shown as the bold red continuous line). (f) Obliquity values (Laskar et al., 2004). (g) Austral summer (December–February) insolation values for 15° S (Laskar et al., 2004). Note that austral summer insolation at this latitude is positively related to precession. Calibrated ¹⁴C accelerator mass spectrometry ages with 2 sigma error of core M125-95-3 are indicated by squares on the lower axis. The grey bar indicates the Heinrich Stadial (HS) 4 to 1. Error bars in the isotope records indicate the standard deviation of replicate analyses. (For interpretation of the references to color in this figure legend, the reader is referred to the Web version of this article).

(weakening) in the Hadley Cell of the winter (summer) hemisphere during maximum obliquity. This strengthening increases the cross-equatorial moisture transport into the summer hemisphere, pushes the ITCZ towards or further into the summer hemisphere and increases the strength of trade winds in the winter hemisphere (Liu and Yang, 2003; Lee and Poulsen, 2005; Mantsis et al., 2014; Bosmans et al., 2015). This phenomenon has a marked influence, for example, in the North African and Asian monsoon systems, where the maximum obliquity coincides with substantial positive precipitation anomalies (e.g., Mantsis et al., 2014; Mohtadi et al., 2016).

Our δ¹³C_{wax} record indicates that the changes in the distribution of C₃ versus C₄ vegetation in the SFRB during the last ca. 45 kyr occurs nearly in phase with the gradual variation in obliquity

(Fig. 3e, f), with expanded C₄ vegetation (i.e., savanna + grassland formations) under minimum obliquity (ca. 29 ka BP) and expanded C₃ vegetation (i.e., forest formations) under maximum obliquity (ca. 15 ka BP). We suggest that this shift from savanna + grassland formations (ca. 29 ka BP) to forest formations (ca. 15 ka BP) was related to a decrease in DSL. Moreover, both processes occurred gradually and followed an increase in obliquity. Comparison of our δ¹³C_{wax} record with atmospheric CO₂ concentrations from ice cores (Bereiter et al., 2015) do not show a clear relation between vegetation changes and pCO₂ (Fig. 3a). While atmospheric CO₂ levels remained stable in the mid-Holocene and late Holocene, the main vegetation composition shifted between the predominance of trees and grasses (Fig. 3a, e). Therefore, we conclude that pCO₂ only has a

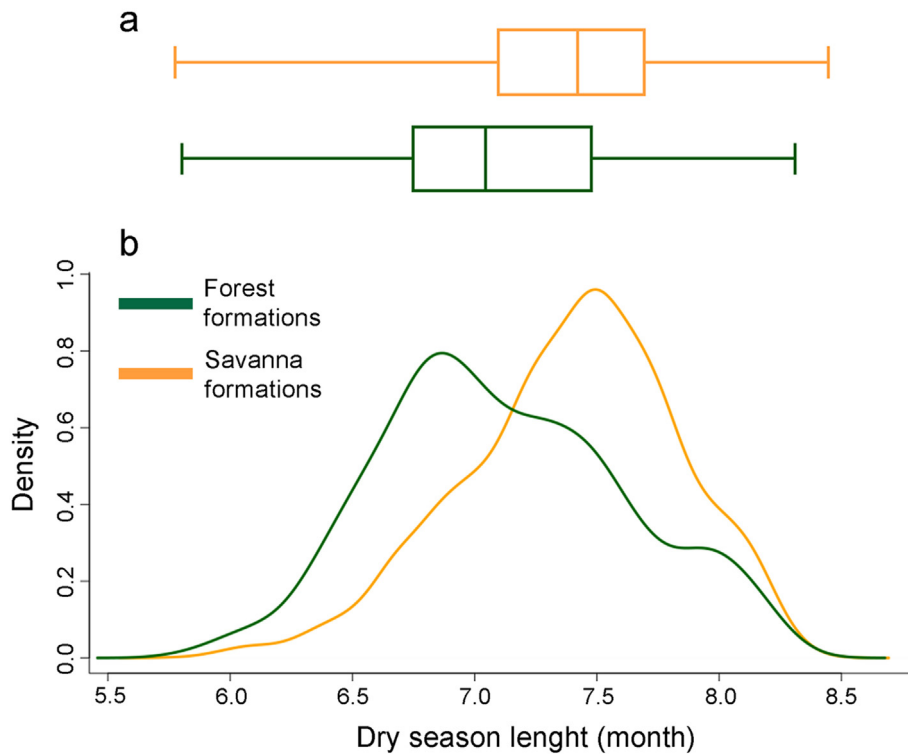


Fig. 4. Distribution of the dry season length (DSL) (Funk et al., 2015) in forest formations and savanna formations (i.e., savanna + grasslands formations) domains (Souza et al., 2020) over eastern tropical South America (i.e., 7–22° S, 48–36° W), encompassing the São Francisco River drainage basin. (a) Box plots of the DSL for forest formations and savanna formations. (b) Density plots of the DSL forest formations and savanna formations. (For interpretation of the references to color in this figure legend, the reader is referred to the Web version of this article).

secondary effect of C_3/C_4 plant occurrence in tropical and subtropical ecosystems.

The CESM experiments ($O_{\max} - O_{\min}$) suggest that a decrease in the DSL over the SFRB from ca. 29 to 15 ka BP was caused by an increase in austral autumn precipitation (Fig. 5b), when the transition from wet to dry season takes place. The change in autumn rainfall is associated with a reorganization of the Hadley Cell and a southward shift of the ITCZ triggered by the obliquity-induced anomalous heating (cooling) of the summer (winter) hemisphere in combination with a delayed (1–2 months) response of the climate system, e.g., due to thermal inertia of the surface ocean. During austral spring, the transition phase from dry to wet season, the effect of obliquity on the tropical rain belt is too far north to have an effect on the SFRB region (Fig. 5c). Indeed, Singarayer et al. (2017) suggested a southward migration of the South Atlantic equatorial rain belt during periods of maximum obliquity in response to variations in the interhemispheric temperature gradient. In summary, high obliquity results in a shortening of the DSL in the SFRB due to enhanced austral autumn precipitation.

In order to test our suggestion that DSL is able to control the extent of forest formations (C_3) versus savanna + grassland formations (C_4) in the SFRB, we compared the modern distribution of these vegetation types (Souza et al., 2020) to instrumental DSL data (Funk et al., 2015) from the area 7–22° S, 48–36° W that encompasses the SFRB (Fig. 4). Our results indicate that both savanna + grassland and forest formations can occur under mean annual precipitation values higher than 1000 mm/yr, and the predominance of one or the other vegetation type depends on the DSL. We find that in areas dominated by forest formations the median DSL is 7.0 months, while in areas dominated by savanna + grassland formations the median DSL is 7.4 months. This indicates that a higher DSL increase the stability of savanna + grassland formations,

and that even a small decrease (increase) in DSL is enough to foster the spread of forest formations (savanna + grassland formations) in the SFRB.

The SFRB is mainly covered by the Cerrado and Caatinga biomes. Forest formations are present in both biomes and, alone, our $\delta^{13}C_{\text{wax}}$ record does not allow us to distinguish between these two vegetation types. As a type of tropical dry forest and shrubland, Caatinga shows a predominance of C_3 type vegetation (Mooney et al., 1989). In the SFRB, this biome typically occurs in regions receiving less than 1000 mm of mean annual precipitation with irregular yearly distribution (Sampaio, 1995). Caatinga occupies the northern portion of the SFRB, where landforms are dominated by relatively small slope angles (Fig. S1) and climate is characterized by the basin-wide lowest mean annual precipitation values (Fig. 1a). These two environmental parameters suggest that the northern portion of the SFRB is not the main source of the sediments delivered by the São Francisco River to the South Atlantic. In contrast, the central and southern portions of the SFRB, dominated by Cerrado (Fig. 1c), show the highest slope angles (Fig. S1) and mean annual precipitation (Fig. 1a) values, being likely the main sediment sources within the SFRB. Thus, we do not expect a substantial amount of Caatinga-derived sediment to reach our core site, making our $\delta^{13}C_{\text{wax}}$ record an indicator of tree cover in Cerrado.

The $\Delta\delta^{13}C_{31-29}$ has been suggested to reflect species richness (Magill et al., 2019). C_3 vegetation presents higher concentrations of species producing C_{29} *n*-alkanes, while C_4 vegetation presents higher concentrations of species producing C_{31} *n*-alkanes (Garcin et al., 2014). Thus, the occurrence of the highest $\Delta\delta^{13}C_{31-29}$ values of our record (Fig. 2c) during minimum obliquity and maximum DSL, suggests the occurrence of diverse vegetation types containing both C_3 and C_4 metabolism. This is a characteristic of an

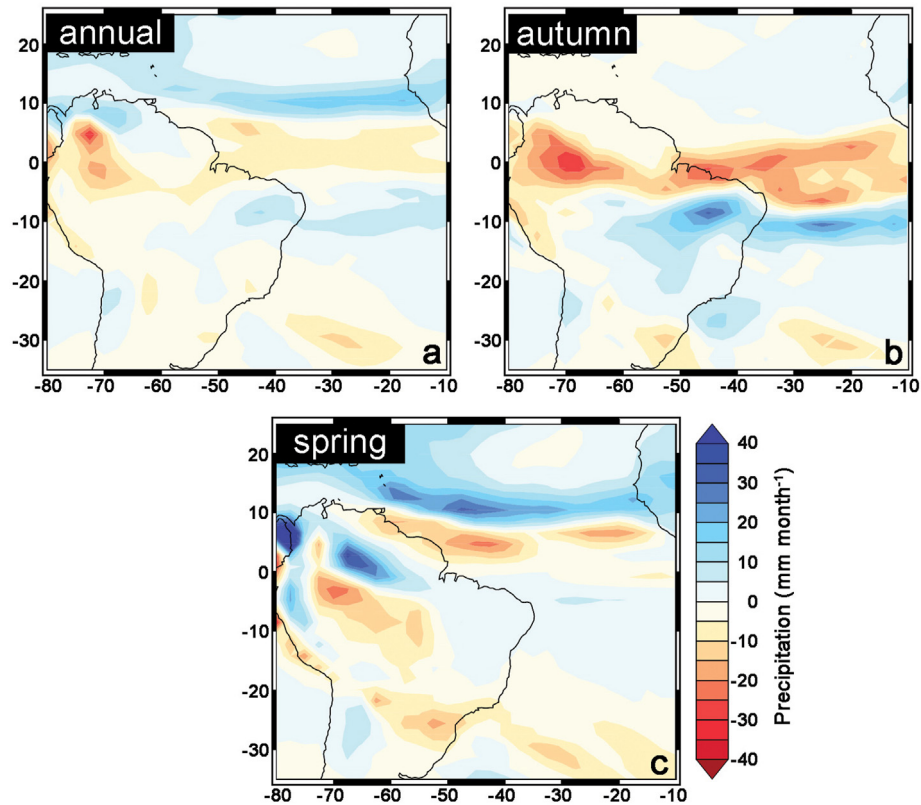


Fig. 5. Precipitation difference between the maximum obliquity and the minimum obliquity ($O_{\max} - O_{\min}$) experiments performed with the Community Earth System Model (version 1.2.2) over South America and the adjacent Atlantic Ocean for (a) annual mean, (b) austral autumn (March–May) and (c) austral spring (September–November). (For interpretation of the references to color in this figure legend, the reader is referred to the Web version of this article).

environment with trees and grasses, a characteristic of the Cerrado biome (Bridgewater et al., 2004) and not of the Caatinga biome (Sampaio, 1995). Likewise, the decrease of $\Delta\delta^{13}\text{C}_{31-29}$ from ca. 29 ka BP (minimum obliquity) to ca. 13 ka BP (maximum obliquity) alongside the decrease in DSL indicate a synchronous increase in C_3 vegetation probably linked to the increase of trees (forest formations) in Cerrado.

Past obliquity-induced changes in the intra-hemispheric meridional insolation gradient (and, consequently, in the surface temperature gradient) bear similarities to projected changes in the intra-hemispheric meridional surface temperature gradient due to global warming (Mantsis et al., 2014). Indeed, some climate models indicate a widening and weakening of the Hadley Cell by the end of the century (Lu et al., 2008; Collins et al., 2013), that resemble to past periods of minimum obliquity (Mantsis et al., 2014). It is also expected that the contrast between wet and dry seasons will increase over most parts of the globe (Collins et al., 2013). In the semiarid northeastern Brazil, projections indicate an increase in droughts and aridity (Marengo and Bernasconi, 2015; Marengo et al., 2017). These anticipated changes would likely increase the DSL, negatively affecting the distribution of trees. Paleoenvironmental records, as our $\delta^{13}\text{C}_{\text{wax}}$ record, provide a long-term perspective on understanding the controls, magnitudes, and spatial/temporal aspects of ecological changes in tropical ecosystem.

5.2. Millennial-scale forcing

Millennial-scale precipitation anomalies in the SFRB are well described in the literature (Stríkis et al., 2015, 2018; Campos et al., 2019). According to Campos et al. (2019), positive precipitation

anomalies over the SFRB during HS are associated with increased austral summer rainfall over eastern tropical South America due to an anomalous cyclonic circulation and moisture transport from the warmer South Atlantic onto the continent.

Indeed, our $\delta\text{D}_{\text{wax}}$ record indicates increases in precipitation intensity over the SFRB during HS4–HS1 (Fig. 3d). The new record bears some advantages in relation to previously existing hydroclimate indicators. First, the $\ln(\text{Ti}/\text{Ca})$ data used in Campos et al. (2019) to infer changes in precipitation in the SFRB indicates the proportion of terrigenous versus biogenic sedimentation, influenced by erosion rates and sea level (Govin et al., 2012). Second, speleothem $\delta^{18}\text{O}$ used in Stríkis et al. (2015, 2018) register conditions at the specific location of the sampled caves. Instead, our $\delta\text{D}_{\text{wax}}$ data is a direct indicator of precipitation intensity (Sachse et al., 2012) and provides a signal that integrates extensive portions of the SFRB.

Our $\delta^{13}\text{C}_{\text{wax}}$ data suggest that millennial scale changes in vegetation in the SFRB are modulated by obliquity, and different HS show a distinct response depending on the obliquity phase (Fig. 3e). HS4 and HS1 occurred during high obliquity when DSL was shorter. Under this obliquity configuration, increased austral summer precipitation fostered forest formations (C_3) to spread throughout the basin. On the other hand, HS3 and HS2 occurred during low obliquity, when DSL was long. This obliquity configuration led to savanna + grassland formations (C_4) to spread even under increased austral summer precipitation.

These variations in the strength of wet season precipitation during HS thus, did not lead to changes in tree cover, as did the gradual shifts induced by obliquity (Fig. 3d, e). Instead, the response of vegetation during the millennial precipitation changes indicates that seasonality primarily determines the response of vegetation to

variations in wet season intensity (Kuechler et al., 2013). This corroborates our suggestion that the DSL is the driving factor in the long-term distribution of forests versus savanna + grasslands formations in eastern tropical South America.

6. Conclusions

We present long-chain *n*-alkanes δD_{wax} and $\delta^{13}C_{wax}$ records from a marine sediment core collected off the SFRB mouth, in eastern tropical South America. Additionally, we compared our findings with modern hydroclimate seasonality (i.e., DSL) and the distribution of vegetation types (i.e., forest, savanna and grassland formations) in the SFRB area. To test our paleoclimatic interpretations, we performed experiments with the CESM. Our δD_{wax} record shows no orbital signal but clear negative excursions during HS, indicating higher rainfall intensities associated to these events. In contrast, the $\delta^{13}C_{wax}$ record shows a marked obliquity pacing but varying responses in the millennial-scale variability. We find no correlation between $\delta^{13}C_{wax}$ and atmospheric CO₂ concentration. For the first time, we describe that obliquity influences vegetation changes in eastern tropical South America through its control on the DSL. Our CESM experiments indicate that on orbital timescales, an increase in obliquity leads to a decrease in the DSL due to an increase in austral autumn precipitation. This change in seasonality triggers an expansion of tree coverage, whereas a decrease in obliquity causes the DSL to increase and reducing tree coverage. On millennial timescales, we show that increases in austral summer precipitation over eastern tropical South America led to varying vegetation responses, depending on the seasonality configuration modulated by obliquity. Although wet season precipitation (as in millennial-scale changes) may influence the density of trees, the DSL (as in orbital-scale changes) is the major control of tree cover in the SFRB.

Credit author statement

Jaqueline Q. Ferreira: conceptualization, data curation, formal analysis, investigation, methodology, validation, visualization, writing – original draft, writing – review & editing. Cristiano M. Chiessi: conceptualization, funding acquisition, project administration, supervision, validation, visualization, writing – original draft, writing – review & editing. Marina Hirota: data curation, formal analysis, software, visualization, writing – review & editing. Rafael S. Oliveira: conceptualization, writing – review & editing. Matthias Prange: formal analysis, resources, software, visualization, writing – review & editing. Christoph Häggi: conceptualization, writing – review & editing. Stefano Crivellari: data curation, visualization. Sri D. Nandini-Weiss: formal analysis, software, visualization, writing – review & editing. Dailson J. Bertassoli Jr, Marília C. Campos, and Stefan Mulitza: writing – review & editing. Ana Luiza S. Albuquerque, André Bahr: resources, writing – review & editing. Enno Schefuß: conceptualization, validation, investigation, writing – review & editing, supervision.

Declaration of competing interest

The authors declare that they have no known competing financial interests or personal relationships that could have appeared to influence the work reported in this paper.

Acknowledgements

The authors thank one anonymous reviewer as well as the editor for their valuable suggestions that improved the manuscript. Logistic and technical assistance was provided by the captain and

crew of the R/V Meteor. New data shown herein will be archived in Pangaea. J. Q. Ferreira acknowledges the financial support from Coordination for the Improvement of Higher Education Personnel (CAPES) (grant 88882.328049/2019–01). C. M. Chiessi acknowledges the financial support from São Paulo Research Foundation (FAPESP) (grants 2018/15123–4 and 2019/24349–9), CAPES (grant 88881.313535/2019–01), National Council for Scientific and Technological Development (CNPq) (grant 312458/2020–7), and the Alexander von Humboldt-Stiftung. D. J. Bertassoli acknowledges the support from FAPESP (grant 2019/24977–0). M. Hirota is currently supported by Serrapilheira Institute (grant Serra-1709-18983). C. Häggi is supported by Swiss National Science Foundation (SNF) (grants P400P2_183856 and P4P4P2_199220). M. C. Campos acknowledges the financial support from FAPESP (grants 2016/10242–0 and 2019/25179–0). A. L. Albuquerque acknowledges the financial support from CAPES (CLIMATE- PrInT grant 88887.310301/2018–00) and CNPq (grants 429767/2018–8 and 302521/2017–8). The isotope analyses were supported by the DFG-Research Center/Cluster of Excellence, “The Ocean Floor – Earth’s Uncharted Interface” at MARUM - Center for Marine Environmental Sciences. We thank Ralph Kreutz for technical support.

Appendix A. Supplementary data

Supplementary data to this article can be found online at <https://doi.org/10.1016/j.quascirev.2022.107402>.

References

- ANA - Agência Nacional de Águas - Superintendência de Planejamento de Recursos Hídricos, 2015. *Conjuntura Dos Recursos Hídricos No Brasil: Regiões Hidrográficas Brasileiras – Edição Especial*.
- Bahr, A., Albuquerque, A.L.S., Ardenghi, N., Batenburg, S.J., Bayer, M., Catunda, M.C., Conforti, A., Dias, B., Ramos, R.D., Egger, L.M., Evers, F., Fischer, T., Hatsukano, K., Hennrich, B., Hoffmann, J., Jivcov, S., Kusch, S., Munz, P., Niedermeier, E., Osborne, A., Raddatz, J., Raeke, A.W., Reissig, S., Sebastian, U., Taniguchi, N., Venancio, I.M., Voigt, S., Wachholz, A., 2016. South American Hydrological Balance and Paleoclimatology during the Late Pleistocene and Holocene (SAMBA), Cruise No. M125. March 21 e April 15, 2016 - Rio de Janeiro (Brazil) e Fortaleza (Brazil). https://doi.org/10.2312/cr_m125.
- Bereiter, B., Eggleston, S., Schmitt, J., Nehrbass-Ahles, C., Stocker, T.F., Fischer, H., Kipfstuhl, S., Chappellaz, J., 2015. Revision of the EPICA Dome C CO₂ record from 800 to 600kyr before present. *Geophys. Res. Lett.* 42 (2), 542–549. <https://doi.org/10.1002/2014GL061957>.
- Bintanja, R., van de Wal, R.S.W., Oerlemans, J., 2005. Modelled atmospheric temperatures and global sea levels over the past million years. *Nature* 437, 125–128. <https://doi.org/10.1038/nature03975>.
- Bird, M.I., Summons, R.E., Gagan, M.K., Roksandic, Z., Dowling, L., Head, J., Fifield, L.K., Cresswell, R.G., Johnson, D.P., 1995. Terrestrial vegetation change inferred from *n*-alkane $\sigma^{13}C$ analysis in the marine environment. *Geochem. Cosmochim. Acta* 59 (13), 2853–2857. [https://doi.org/10.1016/0016-7037\(95\)00160-2](https://doi.org/10.1016/0016-7037(95)00160-2).
- Blaauw, M., Christeny, J.A., 2011. Flexible paleoclimate age-depth models using an autoregressive gamma process. *Bayesian Analysis* 6 (3), 457–474. <https://doi.org/10.1214/11-BA618>.
- Bond, W.J., 2008. What limits trees in C4 grasslands and savannas? *Annu. Rev. Ecol. Evol. Syst.* 39, 641–659. <https://doi.org/10.1146/annurev.ecolsys.39.110707.173411>.
- Bond, W.J., Keeley, J.E., 2005. Fire as a global “herbivore”: the ecology and evolution of flammable ecosystems. *Trends Ecol. Evol.* 20 (7), 387–394. <https://doi.org/10.1016/j.tree.2005.04.025>.
- Bosmans, J.H.C., Hilgen, F.J., Tuenter, E., Lourens, L.J., 2015. Obliquity forcing of low-latitude climate. *Clim. Past* 11 (10), 1335–1346. <https://doi.org/10.5194/cp-11-1335-2015>.
- Braconnot, P., Harrison, S.P., Kageyama, M., Bartlein, P.J., Masson-Delmotte, V., Abe-Ouchi, A., Otto-Bliesner, B., Zhao, Y., 2012. Evaluation of climate models using palaeoclimatic data. *Nat. Clim. Change* 2, 417–424. <https://doi.org/10.1038/nclimate1456>.
- Bragg, F.J., Prentice, I.C., Harrison, S.P., Eglington, G., Foster, P.N., Rommerskirchen, F., Rullkötter, J., 2013. Stable isotope and modelling evidence for CO₂ as a driver of glacial–interglacial vegetation shifts in southern Africa. *Biogeosciences* 10 (3), 2001. <https://doi.org/10.5194/bg-10-2001-2013>, 2010.
- Bridgewater, S., Ratter, J.A., Ribeiro, J.F., 2004. Biogeographic patterns, β -diversity and dominance in the cerrado biome of Brazil. *Biodivers. Conserv.* 13, 2295–2317. <https://doi.org/10.1023/B:BIOC.0000047903.37608.4c>.
- Butzin, M., Köhler, P., Lohmann, G., 2017. Marine radiocarbon reservoir age

- simulations for the past 50,000 years. *Geophys. Res. Lett.* 44 (16), 8473–8480. <https://doi.org/10.1002/2017GL074688>.
- Campos, M.C., Chiessi, C.M., Prange, M., Mulitza, S., Kuhnert, H., Paul, A., Venancio, I.M., Albuquerque, A.L.S., Cruz, F.W., Bahr, A., 2019. A new mechanism for millennial scale positive precipitation anomalies over tropical South America. *Quat. Sci. Rev.* 225, 105990. <https://doi.org/10.1016/j.quascirev.2019.105990>.
- Carvalho, L.M.V., Jones, C., Liebmann, B., 2004. The South Atlantic convergence zone: intensity, form, persistence, and relationships with intraseasonal to interannual activity and extreme rainfall. *J. Clim.* 17 (1), 88–108. [https://doi.org/10.1175/1520-0442\(2004\)017<0088:TSACZL>2.0.CO;2](https://doi.org/10.1175/1520-0442(2004)017<0088:TSACZL>2.0.CO;2).
- Cerling, T.E., Wynn, J.G., Andanje, S.A., Bird, M.I., Korir, D.K., Levin, N.E., Mace, W., Macharia, A.N., Quade, J., Remien, C.H., 2011. Woody cover and hominin environments in the past 6 million years. *Nature* 476, 51–56. <https://doi.org/10.1038/nature10306>.
- Collins, J.A., Schefuß, E., Heslop, D., Mulitza, S., Prange, M., Zabel, M., Tjallingii, R., Dokken, T.M., Huang, E., Mackensen, A., Schulz, M., Tian, J., Zariess, M., Wefer, G., 2011. Interhemispheric symmetry of the tropical African rainbelt over the past 23,000 years. *Nat. Geosci.* 4, 42–45. <https://doi.org/10.1038/ngeo1039>.
- Collins, M., Knutti, R., Arblaster, J., Dufresne, J.L., Fichfet, T., Friedlingstein, P., Gao, X., Gutowski, W.J., Johns, T., Krinner, G., Shongwe, M., Tebaldi, C., Weaver, A.J., Wehner, M.F., Allen, M.R., Andrews, T., Beyerle, U., Bitz, C.M., Bony, S., Booth, B.B.B., 2013. Long-term climate change: projections, commitments and irreversibility. In: Stocker, T.F., Qin, D., Plattner, G.-K., Tignor, M.M.B., Allen, S.K., Boschung, J., Nauels, A., Xia, Y., Bex, V., Midgley, P.M. (Eds.). *Climate Change 2013 - the Physical Science Basis: Contribution of Working Group I to the Fifth Assessment Report of the Intergovernmental Panel on Climate Change*. Intergovernmental Panel on Climate Change. Cambridge University Press, New York NY USA, pp. 1029–1136. <https://doi.org/10.1017/CBO9781107415324.024>.
- Cranwell, P.A., 1981. Diagenesis of free and bound lipids in terrestrial detritus deposited in lacustrine sediment. *Org. Geochem.* 3, 79–89. [https://doi.org/10.1016/0146-6380\(81\)90002-4](https://doi.org/10.1016/0146-6380(81)90002-4).
- Cruz, F.W., Burns, S.J., Karmann, I., Sharp, W.D., Vuille, M., Cardoso, A.O., Ferrari, J.A., Silva Dias, P.L., Viana, O., 2005. Insolation-driven changes in atmospheric circulation over the past 116,000 years in subtropical Brazil. *Nature* 434, 63–66. <https://doi.org/10.1038/nature03365>.
- Cruz, F.W., Vuille, M., Burns, S.J., Wang, X., Cheng, H., Werner, M., Lawrence Edwards, R., Karmann, I., Auler, A.S., Nguyen, H., 2009. Orbitally driven east-west antiphasing of South American precipitation. *Nat. Geosci.* 2, 210–214. <https://doi.org/10.1038/ngeo444>.
- Dansgaard, W., 1964. Stable isotopes in precipitation. *Tellus* 16, 436–463. <https://doi.org/10.3402/tellusa.v16i4.8993>.
- Dubois, N., Oppo, D., Galy, V., Mohtadi, M., Kaars, S., Tierney, J.E., Rosenthal, Y., Eglinton, T.I., Lückge, A., Linsley, B., 2014. Indonesian vegetation response to changes in rainfall seasonality over the past 25,000 years. *Nat. Geosci.* 7, 513–517. <https://doi.org/10.1038/ngeo2182>.
- Ehleringer, J., Cerling, T., Helliker, B., 1997. C4 photosynthesis, atmospheric CO₂, and climate. *Oecologia* 112, 285–299. <https://doi.org/10.1007/s004420050311>.
- Funk, C., Peterson, P., Landsfeld, M., Pedreros, D., Verdin, J., Shukla, S., Husak, G., Rowland, J., Harrison, L., Hoell, A., Michaelsen, J., 2015. The climate hazards infrared precipitation with stations - a new environmental record for monitoring extremes. *Sci. Data* 2, 1–21. <https://doi.org/10.1038/sdata.2015.66>.
- Garcin, Y., Schefuß, E., Schwab, V.F., Garreta, V., Gleixner, G., Vincens, A., Todou, G., Séné, O., Onana, J.M., Achoundong, G., Sachse, D., 2014. Reconstructing C3 and C4 vegetation cover using *n*-alkane carbon isotope ratios in recent lake sediments from Cameroon, Western Central Africa. *Geochem. Cosmochim. Acta* 142, 482–500. <https://doi.org/10.1016/j.gca.2014.07.004>.
- Gomes, H.B., Ambrizzi, T., Herdies, D.L., Hodges, K., Pontes Da Silva, B.F., 2015. Easterly wave disturbances over Northeast Brazil: an observational analysis. *Adv. Meteorol.* 176238. <https://doi.org/10.1155/2015/176238>, 2015.
- Govin, A., Chiessi, C.M., Zabel, M., Sawakuchi, A.O., Heslop, D., Hörner, T., Zhang, Y., Mulitza, S., 2014. Terrigenous input off northern South America driven by changes in Amazonian climate and the North Brazil Current retroreflection during the last 250 ka. *Clim. Past* 10, 843–862. <https://doi.org/10.5194/cp-10-843-2014>.
- Govin, A., Holzwarth, U., Heslop, D., Keeling, L.F., Zabel, M., Mulitza, S., Collins, J.A., Chiessi, C.M., 2012. Distribution of major elements in Atlantic surface sediments (36°N–49°S): imprint of terrigenous input and continental weathering. *G-cubed* 13 (1), 1–23. <https://doi.org/10.1029/2011GC003785>.
- Häggi, C., Chiessi, C.M., Merkel, U., Mulitza, S., Prange, M., Schulz, M., Schefuß, E., 2017. Response of the Amazon rainforest to late Pleistocene climate variability. *Earth Planet Sci. Lett.* 479, 50–59. <https://doi.org/10.1016/j.epsl.2017.09.013>.
- Harris, I., Osborn, T.J., Jones, P., Lister, D., 2020. Version 4 of the CRU TS monthly high-resolution gridded multivariate climate dataset. *Sci. Data* 7 (1), 1–18. <https://doi.org/10.1038/s41597-020-0453-3>.
- Hirota, M., Holmgren, M., Van Nes, E.H., Scheffer, M., 2011. Global resilience of tropical forest. *Science* 334 (6053), 232–235. <https://doi.org/10.1126/science.1210657>.
- Hirota, M., Nobre, C., Oyama, M.D., Bustamante, M.M.C., 2010. The climatic sensitivity of the forest, savanna and forest-savanna transition in tropical South America. *New Phytol.* 187 (3), 707–719. <https://doi.org/10.1111/j.1469-8137.2010.03352.x>.
- Hoffmann, W.A., Geiger, E.L., Gotsch, S.G., Rossatto, D.R., Silva, L.C.R., Lau, O.L., Haridasan, M., Franco, A.C., 2012. Ecological thresholds at the savanna-forest boundary: how plant traits, resources and fire govern the distribution of tropical biomes. *Ecol. Lett.* 15 (7), 759–768. <https://doi.org/10.1111/j.1461-0248.2012.01789.x>.
- Hou, A., Bahr, A., Raddatz, J., Voigt, S., Greule, M., Albuquerque, A.L., Chiessi, C.M., Friedrich, O., 2020. Insolation and greenhouse gas forcing of the south American monsoon system across three glacial-interglacial cycles. *Geophys. Res. Lett.* 47 (14), 1–10. <https://doi.org/10.1029/2020GL087948>.
- House, J.I., Archer, S., Breshears, D.D., Scholes, R.J., 2003. Conundrums in mixed woody – herbaceous plant systems. *J. Biogeogr.* 30 (11), 1763–1777. <https://doi.org/10.1046/j.1365-2699.2003.00873.x>.
- Hurrell, J.W., Holland, M.M., Gent, P.R., Ghan, S., Kay, J.E., Kushner, P.J., Lamarque, J.F., Large, W.G., Lawrence, D., Lindsay, K., Lipscomb, W.H., Long, M.C., Mahowald, N., Marsh, D.R., Neale, R.B., Rasch, P., Vavrus, S., Vertenstein, M., Bader, D., Collins, W.D., Hack, J.J., Kiehl, J., Marshall, S., 2013. The community earth system model: a framework for collaborative research. *Bull. Am. Meteorol. Soc.* 94 (9), 1339–1360. <https://doi.org/10.1175/BAMS-D-12-00121.1>.
- Jackson, R.B., Banner, J.L., Jobbágy, E.G., Pockman, R.J., Wall, D.H., 2002. Ecosystem carbon loss with woody plant invasion of grasslands. *Nature* 418, 623–626. <https://doi.org/10.1038/nature00910>.
- Kousky, V.E., 1979. Frontal influences on northeast Brazil. *Mon. Weather Rev.* 107 (9), 1140–1153. [https://doi.org/10.1175/1520-0493\(1979\)107<1140:FIONB>2.0.CO;2](https://doi.org/10.1175/1520-0493(1979)107<1140:FIONB>2.0.CO;2).
- Kuechler, R.R., Schefuß, E., Beckmann, B., Dupont, L., Wefer, G., 2013. NW African hydrology and vegetation during the Last Glacial cycle reflected in plant-wax-specific hydrogen and carbon isotopes. *Quat. Sci. Rev.* 82, 56–67. <https://doi.org/10.1016/j.quascirev.2013.10.013>.
- Langner, M., Mulitza, S., 2019. Technical Note: PaleoDataView - a software toolbox for the collection, homogenization and visualization of marine proxy data. *Clim. Past* 15, 2067–2072. <https://doi.org/10.5194/cp-15-2067-2019>.
- Laskar, J., Robutel, P., Joutel, F., Gastineau, M., Correia, A.C.M., Levrard, B., 2004. A long-term numerical solution for the insolation quantities of the Earth. *Astron. Astrophys.* 428 (1), 261–285. <https://doi.org/10.1051/0004-6361:20041335>.
- Lee, J.E., Fung, I., 2008. “Amount effect” of water isotopes and quantitative analysis of post-condensation processes. *Hydrol. Process.* 22 (1), 1–8. <https://doi.org/10.1002/hyp.6637>.
- Lee, S.Y., Poulsen, C.J., 2005. Tropical Pacific climate response to obliquity forcing in the Pleistocene. *Paleoceanography* 20 (4), 1–10. <https://doi.org/10.1029/2005PA001161>.
- Lenters, J.D., Cook, K.H., 1997. On the origin of the Bolivian high and related circulation features of the South American climate. *J. Atmos. Sci.* 54 (5), 656–677. [https://doi.org/10.1175/1520-0469\(1997\)054<0656:otootb>2.0.co;2](https://doi.org/10.1175/1520-0469(1997)054<0656:otootb>2.0.co;2).
- Liu, Z., Yang, H., 2003. Extratropical control of tropical climate, the atmospheric bridge and oceanic tunnel. *Geophys. Res. Lett.* 30 (5), 1230. <https://doi.org/10.1029/2002gl016492>.
- Lu, J., Chen, G., Frierson, D.M.W., 2008. Response of the zonal mean atmospheric circulation to El Niño versus global warming. *J. Clim.* 21 (22), 5835–5851. <https://doi.org/10.1175/2008JCLI2200.1>.
- Magill, C.R., Eglinton, G., Eglinton, T., 2019. Isotopic variance among plant lipid homologues correlates with biodiversity patterns of their source communities. *PLoS One* 14 (2), 1–17. <https://doi.org/10.1371/journal.pone.0212211>.
- Mantsis, D.F., Lintner, B.R., Broccoli, A.J., Erb, M.P., Clement, A.C., Park, H.S., 2014. The response of large-scale circulation to obliquity-induced changes in meridional heating gradients. *J. Clim.* 27 (14), 5504–5516. <https://doi.org/10.1175/JCLI-D-13-00526.1>.
- Marengo, J.A., Bernasconi, M., 2015. Regional differences in aridity/drought conditions over Northeast Brazil: present state and future projections. *Climatic Change* 129, 103–115. <https://doi.org/10.1007/s10584-014-1310-1>.
- Marengo, J.A., Torres, R.R., Alves, L.M., 2017. Drought in Northeast Brazil—past, present, and future. *Theor. Appl. Climatol.* 129, 1189–1200. <https://doi.org/10.1007/s00704-016-1840-8>.
- Mohtadi, M., Prange, M., Steinke, S., 2016. Palaeoclimatic insights into forcing and response of monsoon rainfall. *Nature* 533, 191–199. <https://doi.org/10.1038/nature17450>.
- Mooney, H.A., Bullock, S.H., Ehleringer, J.R., 1989. Carbon isotope ratios of plants of a tropical dry forest in Mexico. *Funct. Ecol.* 3 (2), 137–142. <https://doi.org/10.2307/2389294>.
- Myers, N., Mittermeier, R.A., Mittermeier, C.G., da Fonseca, G.A.B., Kent, J., 2000. Biodiversity hotspots for conservation priorities. *Nature* 403, 853–858. <https://doi.org/10.1038/35002501>.
- Nix, H.A., 1983. In: Bourlière, F. (Ed.), *Climate of Tropical Savannas. Ecosystems of the World: Tropical Savannas*. Elsevier, pp. 37–62.
- Oliveira-Filho, A.T., Fontes, M.A.L., 2000. Patterns of floristic differentiation among atlantic forests in southeastern Brazil and the influence of climate. *Biotropica* 32 (4b), 793–810. <https://doi.org/10.1111/j.1744-7429.2000.tb00619.x>.
- Pausas, J.G., Bond, W.J., 2020. Alternative biome states in terrestrial ecosystems. *Trends Plant Sci.* 25 (3), 250–263. <https://doi.org/10.1016/j.tplants.2019.11.003>.
- Prado, L.F., Wainer, I., Chiessi, C.M., 2013. Mid-holocene PMIP3/CMIP5 model results: Intercomparison for the south American monsoon system. *Holocene* 23 (12), 1915–1920. <https://doi.org/10.1177/0959683613505336>.
- Raymo, M.E., Nisancioglu, K., 2003. The 41 kyr world: milankovitch's other unsolved mystery. *Paleoceanography* 18 (1), 1–6. <https://doi.org/10.1029/2002pa000791>.
- Reimer, P., Austin, W., Bard, E., Bayliss, A., Blackwell, P., Ramsey, C.B., Butzin, M., Cheng, H., Edwards, L.R., Friedrich, M., Grootes, P.M., Guilderson, T.P., Hajdas, I., Heaton, T.K., Hogg, A.G., Hughen, K.A., Kromer, B., Manning, S.W., Muscheler, R., Palmer, J.G., Pearson, C., Plicht, J., Reimer, R.W., Richards, D.A., Scott, E.M.,

- Southon, J.R., Turney, C.S.M., Wacker, L., Adolphi, F., Büntgen, U., Capano, M., Fahrni, S.M., Fogtmann-Schulz, A., Friedrich, R., Köhler, P., Kudsak, S., Miyake, F., Olsen, J., Reinig, F., Sakamoto, M., Sookdeo, A., Talamo, S., 2020. The IntCal20 northern hemisphere radiocarbon age calibration curve (0–55 cal kBP). *Radiocarbon* 62 (4), 725–757. <https://doi.org/10.1017/RDC.2020.41>.
- Riginos, C., Grace, J.B., 2008. Savanna tree density, herbivores, and the herbaceous community: bottom-up vs. top-down effects. *Ecology* 89 (8), 2228–2238. <https://doi.org/10.1890/07-1250.1>.
- Risi, C., Bony, S., Vimeux, F., 2008. Influence of convective processes on the isotopic composition ($\delta^{18}\text{O}$ and δD) of precipitation and water vapor in the tropics: 2. Physical interpretation if the amount effect. *J. Geophys. Res.* 113 (D19), 1–12. <https://doi.org/10.1029/2008JD009943>.
- Sachse, D., Billault, I., Bowen, G.J., Chikaraishi, Y., Dawson, T.E., Feakins, S.J., Freeman, K.H., Magill, C.R., McInerney, F.A., van der Meer, M.T.J., Polissar, P., Robins, R.J., Sachs, J.P., Schmidt, H.L., Sessions, A.L., White, J.W.C., West, J.B., Kahmen, A., 2012. Molecular paleohydrology: interpreting the hydrogen-isotopic composition of lipid biomarkers from photosynthesizing organisms. *Annu. Rev. Earth Planet Sci.* 40, 221–249. <https://doi.org/10.1146/annurev-earth-042711-105535>.
- Sampaio, E.V.S.B., 1995. Overview of the Brazilian caatinga. In: *Seasonally Dry Tropical Forests*. Cambridge University Press, pp. 35–63. <https://doi.org/10.1017/CBO9780511753398.003>.
- Sankaran, M., Ratnam, J., Hanan, N.P., 2004. Tree-grass coexistence in savannas revisited - insights from an examination of assumptions and mechanisms invoked in existing models. *Ecol. Lett.* 7, 480–490. <https://doi.org/10.1111/j.1461-0248.2004.00596.x>.
- Schefuß, E., Schouten, S., Schneider, R., 2005. Climatic controls on central African hydrology during the past 20,000 years. *Nature* 437, 1003–1006. <https://doi.org/10.1038/nature03945>.
- Schefuß, E., Kuhlmann, H., Mollenhauer, G., Prange, M., Pätzold, J., 2011. Forcing of wet phases in southeast Africa over the past 17,000 years. *Nature* 480, 509–512. <https://doi.org/10.1038/nature10685>.
- Schrag, D.P., Adkins, J.F., McIntyre, K., Alexander, J.L., Hodell, D.A., Charles, C.D., McManus, J.F., 2002. The oxygen isotopic composition of seawater during the Last Glacial Maximum. *Quat. Sci. Rev.* 21 (1–3), 331–342. [https://doi.org/10.1016/S0277-3791\(01\)00110-X](https://doi.org/10.1016/S0277-3791(01)00110-X).
- Simioni, G., Gignoux, J., Le Roux, X., 2003. Tree layer spatial structure can affect savanna production and water budget: results of a 3-D model. *Ecology* 84 (7), 1879–1894. [https://doi.org/10.1890/0012-9658\(2003\)084\[1879:TLSSCA\]2.0.CO;2](https://doi.org/10.1890/0012-9658(2003)084[1879:TLSSCA]2.0.CO;2).
- Singarayer, J.S., Valdes, P.J., Roberts, W.H.G., 2017. Ocean dominated expansion and contraction of the late Quaternary tropical rainbelt. *Sci. Rep.* 7, 9382. <https://doi.org/10.1038/s41598-017-09816-8>.
- Souza, C.M., Shimbo, J.Z., Rosa, M.R., Parente, L.L., Alencar, A.A., Rudorff, B.F.T., Hasenack, H., Matsumoto, M., Ferreira, L.G., Souza-Filho, P.W.M., de Oliveira, S.W., Rocha, W.F., Fonseca, A.V., Marques, C.B., Diniz, C.G., Costa, D., Monteiro, D., Rosa, E.R., Véllez-Martin, E., Weber, E.J., Lenti, F.E.B., Paternost, F.F., Pareyn, F.G.C., Siqueira, J.V., Viera, J.L., Neto, L.C.F., Saraiva, M.M., Sales, M.H., Salgado, M.P.G., Vasconcelos, R., Galano, S., Mesquita, V.V., Azevedo, T., 2020. Reconstructing three decades of land use and land cover changes in Brazilian biomes with landsat archive and earth engine. *Rem. Sens.* 12 (17), 2735. <https://doi.org/10.3390/RS12172735>.
- Staver, A.C., Archibald, S., Levin, S.A., 2011. The global extent and determinants of savanna and forest as alternative biome states. *Science* 334 (6053), 230–232. <https://doi.org/10.1126/science.1210465>.
- Stríkis, N.M., Chiessi, C.M., Cruz, F.W., Vuille, M., Cheng, H., De Souza Barreto, E.A., Mollenhauer, G., Kasten, S., Karmann, I., Edwards, R.L., Bernal, J.P., Sales, H.D.R., 2015. Timing and structure of mega-SACZ events during Heinrich stadial 1. *Geophys. Res. Lett.* 42 (13), 5477–5484. <https://doi.org/10.1002/2015GL064048>.
- Stríkis, N.M., Cruz, F.W., Barreto, E.A.S., Naughton, F., Vuille, M., Cheng, H., Voelker, A.H.L., Zhang, H., Karmann, I., Edwards, R.L., Auler, A.S., Santos, R.V., Sales, H.R., 2018. South American monsoon response to iceberg discharge in the North Atlantic. *Proc. Natl. Acad. Sci. Unit. States Am.* 115 (15), 3788–3793. <https://doi.org/10.1073/pnas.1717784115>.
- Tierney, J.E., DeMenocal, P.B., 2013. Abrupt shifts in Horn of Africa hydroclimate since the last glacial maximum. *Science* 342 (6160), 843–846. <https://doi.org/10.1126/science.1240411>.
- Vera, C., Higgins, W., Amador, J., Ambrizzi, T., Garreaud, R., Gochis, D., Gutzler, D., Lettenmaier, D., Marengo, J., Mechoso, C.R., Nogues-Paegle, J., Silva Dias, P.L., Zhang, C., 2006. Toward a unified view of the American monsoon systems. *J. Clim.* 19 (20), 4977–5000. <https://doi.org/10.1175/JCLI3896.1>.